

Phase Transitions in Nonreciprocal Driven-Dissipative Condensates

Ron Belyansky,^{1,*} Cheyne Weis,² Ryo Hanai,³ Peter B. Littlewood,^{2,4} and Aashish A. Clerk¹

¹*Pritzker School of Molecular Engineering, University of Chicago, Chicago, IL 60637, USA*

²*James Franck Institute and Department of Physics, The University of Chicago, Chicago, Illinois 60637, United States*

³*Department of Physics, Institute of Science Tokyo, 2-12-1 Ookayama Meguro-ku, Tokyo, 152-8551, Japan*

⁴*School of Physics and Astronomy, University of St Andrews, N Haugh, St Andrews KY16 9SS, United Kingdom*

(Dated: February 11, 2025)

We investigate the influence of boundaries and spatial nonreciprocity on nonequilibrium driven-dissipative phase transitions. We focus on a one-dimensional lattice of nonlinear bosons described by a Lindblad master equation, where the interplay between coherent and incoherent dynamics generates nonreciprocal interactions between sites. Using a mean-field approach, we analyze the phase diagram under both periodic and open boundary conditions. For periodic boundaries, the system always forms a condensate at nonzero momentum and frequency, resulting in a time-dependent traveling wave pattern. In contrast, open boundaries reveal a far richer phase diagram, featuring multiple static and dynamical phases, as well as exotic phase transitions, including the spontaneous breaking of particle-hole symmetry associated with a critical exceptional point and phases with distinct bulk and edge behavior. Our model avoids post-selection or unphysical non-Hermitian Hamiltonians and is experimentally realizable in platforms such as superconducting circuits.

Introduction.—Driven-dissipative many-body systems have emerged as a versatile platform for exploring novel nonequilibrium phenomena that are inaccessible in equilibrium. These systems exhibit a rich variety of exotic phases of matter and phase transitions, as well as dynamic behaviors unique to nonequilibrium settings [1]. Much of this interest is motivated by the emergence of programmable quantum simulators in various platforms such as exciton-polariton systems in semiconductors [2], ultracold atomic systems [3], photonic platforms [4, 5], and superconducting circuits [6], where both the coherent interactions and dissipation can be engineered to a degree.

Recent years have seen a surge of interest in nonreciprocally interacting many-body systems, especially the nonequilibrium phases that emerge therein. Prototypical examples often consist of multi-species systems where the interactions between different species are asymmetric [7–14]. Nonreciprocal interactions have also been shown to give rise to exotic nonequilibrium phases of matter, such as long-range order in two spatial dimensions [15–17], time-crystalline order [8, 10–12, 14], nonequilibrium boundary modes [18], and chaotic phases [19]. These phenomena have attracted significant attention in diverse fields such as active matter [20], biology [21], and neural networks [22], with early explorations of analogous quantum systems also beginning to emerge [23–27].

Another example of nonreciprocity arises when a system exhibits preferred spatial directionality. A paradigmatic example is the Hatano-Nelson model [28, 29], a one-dimensional system governed by a non-Hermitian Hamiltonian with asymmetric left and right hopping rates. This asymmetry leads to exponential localization of all eigenstates at one boundary under open boundary

conditions (OBC), while under periodic boundary conditions (PBC), the eigenstates remain extended—a phenomenon known as the non-Hermitian skin effect (NHSE) [30–32]. While recent studies have explored nonlinear extensions of such models [27, 33–39], the impact on phase transitions and the specific role of boundaries, particularly beyond the framework of non-Hermitian Hamiltonians, remains largely underexplored.

In this work, we investigate the effect of nonreciprocity and the NHSE in the presence of interactions on nonequilibrium phase transitions. We focus on a mean-field treatment of driven-dissipative condensates in one

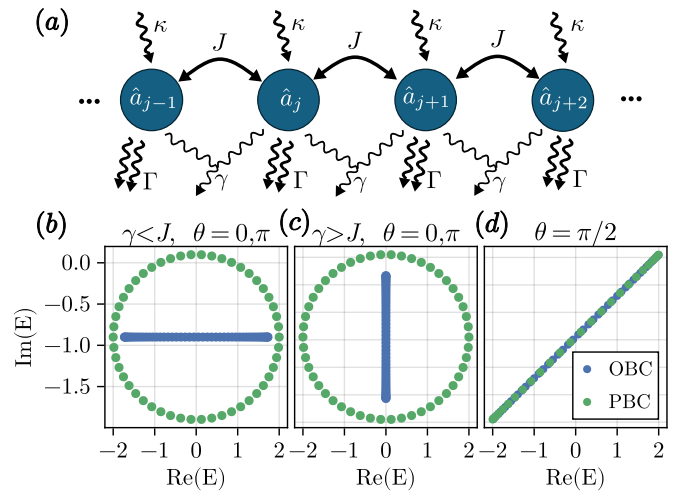


FIG. 1. (a) Schematic illustration of the system. (b, c) Spectrum of the Hatano-Nelson Hamiltonian Eq. (1) in the regime of maximal nonreciprocity. (d) Spectrum in the reciprocal case.

dimension, described by a Lindblad master equation, and find that the steady-state phase diagram is highly sensitive to boundary conditions. While periodic boundary conditions lead to a single phase characterized by a finite momentum and frequency condensate, open boundaries result in a rich variety of static and dynamical phases. This includes exotic phase transitions associated with particle-hole symmetry breaking and critical exceptional points (CEPs) [9, 12, 13, 24, 25, 40–44], as well as phases with distinct bulk and edge dynamics. Our work suggests that the NHSE affects physics in a rich dynamic manner due to the interplay between nonreciprocity and nonlinearity.

Model.—We consider a chain (or a ring) of bosonic sites [see Fig. 1(a)] described by a quantum master equation [45] $\partial_t \hat{\rho} = -i[\hat{H}, \hat{\rho}] + \sum_{\mu=1,2,3} \sum_j \mathcal{D}[\hat{L}_j^{(\mu)}] \hat{\rho}$ where the Hamiltonian, $\hat{H} = -J \sum_j (\hat{a}_j^\dagger \hat{a}_{j+1} + \hat{a}_{j+1}^\dagger \hat{a}_j)$ describes hoppings with rate J , where \hat{a}_j and \hat{a}_j^\dagger are the site- j creation and annihilation operators. The dissipators $D[\hat{L}] \hat{\rho} = \hat{L}^\dagger \hat{\rho} \hat{L} - \frac{1}{2} \{ \hat{L}^\dagger \hat{L}, \hat{\rho} \}$ describe three types of incoherent processes: single particle pumping with rate κ ($\hat{L}_j^{(1)} = \sqrt{2\kappa} \hat{a}_j^\dagger$), two particle decay with rate Γ ($\hat{L}_j^{(2)} = \sqrt{2\Gamma} \hat{a}_j^2$), and correlated single particle decay with rate γ ($\hat{L}_j^{(3)} = \sqrt{2\gamma} (\hat{a}_j - ie^{i\theta} \hat{a}_{j+1})$).

At the quadratic level (i.e., $\Gamma = 0$), this realizes the dissipative version of the Hatano-Nelson model [46–48]. This can be seen, for example, from the Heisenberg equations of motion $i\partial_t \hat{a}_n = \sum_m (H_{\text{HN}})_{nm} \hat{a}_m$ where the (single-particle) Hatano-Nelson Hamiltonian H_{HN} is

$$H_{\text{HN}} = \sum_j (\Delta |j\rangle\langle j| + J_+ |j\rangle\langle j+1| + J_- |j\rangle\langle j-1|), \quad (1)$$

where $\Delta = i(\kappa - 2\gamma)$, $J_+ = -(J + \gamma e^{i\theta})$, $J_- = -(J - \gamma e^{-i\theta})$. The interplay between the coherent dynamics (J) and the correlated loss (γ) generates asymmetric hoppings rates $J_+ \neq J_-$, favoring left- (right-) propagating modes when $\theta = 0$ ($\theta = \pi$). The NHSE is reflected in the spectrum of Eq. (1), illustrated in Fig. 1(b,c,d). The PBC spectrum is an ellipse in the complex plane, whereas for OBC the spectrum always falls on a line [see Fig. 1(b,c)]. For $\theta = \pm\pi/2$, the model is reciprocal (i.e. $|J_+| = |J_-|$), and the ellipse shrinks into a line signaling the absence of the NHSE [see Fig. 1(d)].

The quadratic system without two-particle losses can be dynamically unstable; with these interaction terms ($\Gamma \neq 0$) the system is always stable and becomes genuinely many-body. Here, we study the mean-field dynamics of the Lindbladian, described by the equation of motion (EOM)

$$i\partial_t \alpha_j = i(\kappa - 2\gamma)\alpha_j - i\Gamma|\alpha_j|^2 \alpha_j - (J + \gamma e^{i\theta})\alpha_{j+1} - (J - \gamma e^{-i\theta})\alpha_{j-1}, \quad (2)$$

where $\alpha_j \equiv \langle a_j \rangle$ is the coherent state amplitude on each site. In the reciprocal case, $\theta = -\pi/2$, Eq. (2) is equiv-

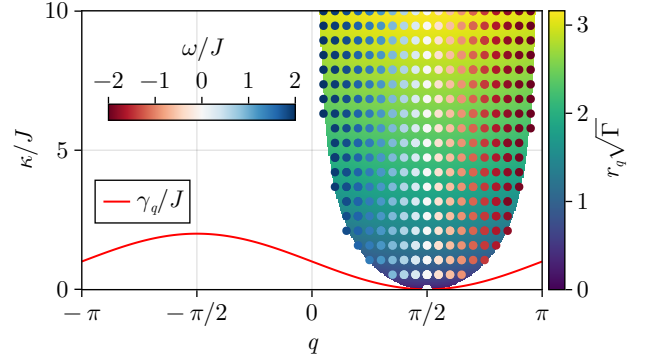


FIG. 2. Stability diagram of the PBC solutions in Eq. (4) for $\theta = \pi, \gamma/J = 0.5$. Colored region corresponds to the stable solutions for $N \rightarrow \infty$, with the color corresponding to the amplitude r_q . Dots correspond to stable solutions for a finite system of $N = 40$, with the color showing the oscillation frequency ω_q [Eq. (3)]. Red line is the momentum decay rate [Eq. (3)].

alent to a discrete Gross-Pitaevskii equation, which is frequently used in the study of driven-dissipative condensates [49–53].

Periodic boundary conditions.—We begin with a study of the steady-state solutions of Eq. (2) with PBC, i.e., $\alpha_{N+1} = \alpha_1$. One finds that for large N , the vacuum state $\alpha_j = 0$ is unstable for any amount of pumping $\kappa > 0$. This can be seen from the spectrum of Eq. (1) which is diagonalized in momentum space $H_{\text{HN}} = \sum_q (i\kappa - i\gamma_q + \omega_q) |q\rangle\langle q|$ where

$$\gamma_q = 2\gamma(1 + \sin(q + \theta)), \quad \omega_q = -2J \cos(q), \quad (3)$$

are the decay rate and energy for momentum $q = 2\pi m/N$, $m = 0, \dots, N-1$. For any choice of θ , the mode at $q + \theta = -\pi/2$ (which is a dark mode of all $\hat{L}_j^{(2)}$ dissipators) experiences no dissipation and can be excited with infinitesimal κ (for $N \rightarrow \infty$).

The nonlinearity in Eq. (2) couples the plane wave solutions of the linear system, and one might expect that full behavior of the nonlinear equations would thus be more complex. This is not the case: the time-dependent traveling wave states (i.e. finite momentum condensates)

$$\alpha_j(t) = r_q e^{iqj - i\omega_q t}, \quad r_q = \sqrt{\frac{\kappa - \gamma_q}{\Gamma}}, \quad (4)$$

are solutions of Eq. (2) with PBC whenever $\gamma_q < \kappa$. Not all of these plane-wave solutions are stable: a momentum- q traveling wave can become unstable against creation of pairs at momenta $q \pm k$, for some k that depends on κ and γ [see Supplemental Material (SM) for details [54]]. Figure 2 shows the resulting stability diagram for $\theta = \pi$ and $\gamma/J = 0.5$. For $\kappa \rightarrow 0$, only the q^* mode such that $\gamma_{q^*} \rightarrow 0$ is stable ($q^* = \pi/2$ for $\theta = \pi$), as expected. As $\kappa \rightarrow \infty$, on the other hand, all the modes in a range of π

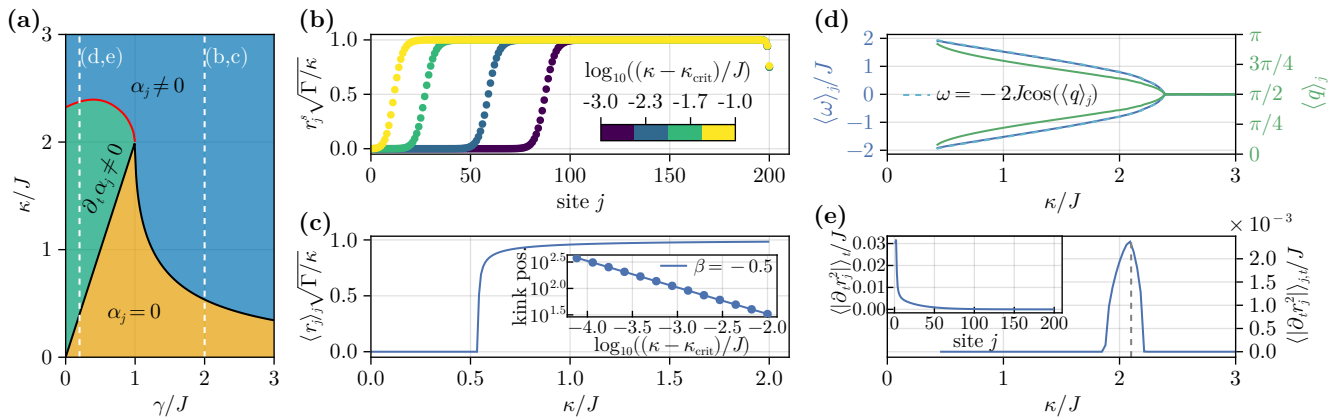


FIG. 3. (a) Steady-state OBC phase diagram for $\theta = 0, \pi$. Dashed lines at $\gamma/J = 0.2$ and $\gamma/J = 2$ correspond to line cuts shown in panels (d, e) and (b, c), respectively. (b) Spatial profile of the amplitude in the static condensate phase for different values of κ near the phase transition for $\gamma/J = 2, \theta = \pi$. (c) Average amplitude as a function of κ . The inset shows the kink position near the phase transition, with the solid line representing a power-law fit yielding a critical exponent $\beta = -0.5$. (d) Average frequency (left axis, blue) and average wavevector (right axis, green) as functions of κ/J for $\gamma/J = 0.2, \theta = \pi$. The dashed line (overlapping with the numerically obtained solid blue line) represents the PBC dispersion from Eq. (3). (e) Time and space average of the magnitude of the rate of change of density as a function of κ . The inset shows the spatial profile of the time-averaged density rate of change at $\kappa/J = 2.1$ (dashed line).

centered about $q^* = -\pi/2 - \theta$ are stable (corresponding to all the right-moving modes for $\theta = \pi$). Numerically, we find these simple traveling waves appear to be the only possible behavior at long times. For PBC and $\theta = \pi$, we thus find that the system always condenses into a single finite momentum mode (chosen by the initial conditions from a range of possible positive momenta), with a frequency ω_q that is non-zero (unless $q = \pi/2$). Other choices of θ lead to qualitatively similar results, with everything in Fig. 2 shifted to $q^* = -\pi/2 - \theta$. Analogous traveling wave solutions also appear in the complex Landau-Ginzburg equation [55, 56], the continuum version of the reciprocal $\theta = -\pi/2$ limit of our model, where the stable possible condensates are centered about $q^* = 0$.

Open boundary conditions.—For PBC, the angle θ (and hence the nonreciprocity $|J_+| - |J_-|$) does not play a significant role. In contrast, for OBC, the value of θ is crucial to the physics. At $\theta = 0, \pi$, the hopping is maximally nonreciprocal, and the full nonlinear system has an antilinear \mathbb{Z}_2 particle-hole \mathcal{PH} symmetry. At the level of the EOM Eq. (2), this symmetry implies that if $\alpha_j(t)$ is a solution, then so is $e^{i\pi j} \alpha_j^*(t)$. We will demonstrate below that this symmetry can be spontaneously broken for OBC. At the level of the linear $\Gamma = 0$ theory, this symmetry transforms the quadratic Hatano-Nelson Hamiltonian as $(\mathcal{PH})H_{\text{HN}}(\mathcal{PH})^{-1} = -H_{\text{HN}}$ [57]. In contrast, for more general $\theta \neq 0, \pi$, the \mathcal{PH} symmetry is explicitly broken, making nontrivial steady states time-dependent. Here, we focus on the \mathcal{PH} -symmetric, maximally nonreciprocal case of $\theta = 0, \pi$, choosing $\theta = \pi$ for concreteness. The corresponding phase diagram is shown in Fig. 3(a).

The first intriguing feature of the OBC phase diagram is that the vacuum solution, $\alpha_j = 0$, becomes stable within a certain range of parameters, shown in yellow in Fig. 3(a). This is in sharp contrast to the PBC case, where the vacuum is always unstable for finite pumping. The linear stability of the OBC vacuum phase is determined by examining the imaginary parts of the eigenvalues of Eq. (1) with OBC. The spectrum of Eq. (1) differs qualitatively depending on whether $\gamma < J$ or $\gamma > J$ [see Fig. 1(b, c)], with $\gamma = J$ marking an N -th order exceptional point. The eigenvalues are given by

$$E_m = \begin{cases} i(\kappa - 2\gamma) + 2\sqrt{J^2 - \gamma^2} \cos(q_m) & \text{for } \gamma < J, \\ i[\kappa - 2\gamma + 2\sqrt{\gamma^2 - J^2} \cos(q_m)] & \text{for } \gamma > J, \end{cases} \quad (5)$$

where $q_m = \pi m/(N+1)$, $m = 1, \dots, N$. For $\gamma < J$, all eigenstates have the same damping rate, and the phase transition occurs at $\kappa_{\text{crit}} = 2\gamma$ [black line in Fig. 3(a)] where all linear modes become unstable simultaneously. For $\gamma > J$, the $m = 1$ mode ($q \rightarrow 0$ in the thermodynamic limit) is the first to become unstable, yielding the critical value $\kappa_{\text{crit}} = 2\gamma - 2\sqrt{\gamma^2 - J^2}$.

For $\gamma > J$, as κ is increased above κ_{crit} , the system undergoes a continuous phase transition from the vacuum phase ($\langle \alpha_j \rangle_j = 0$) to a time-independent static condensate [blue region in Fig. 3(a)] with $\langle \alpha_j \rangle_j \neq 0$ [Fig. 3(c)], where $\langle o \rangle_j$ denotes the spatial average of o . Up to a spontaneously chosen global $U(1)$ phase, the complex amplitudes in the static phase are given by $\alpha_j^s = r_j^s e^{iq_s j}$, where $q_s = \pi/2$ ($-\pi/2$) for $\theta = \pi$ ($\theta = 0$). Interestingly, this phase order corresponds to the minimal-damping wavevector of the PBC system in Eq. (3). This

finite-momentum condensate emerges as κ increases in the form of a kink that sweeps across the system from right to left [see Fig. 3(b)]. Numerically, we find that the height of the kink is $\sqrt{\kappa/\Gamma}$. In fact, the uniform state $\alpha_j = \sqrt{\kappa/\Gamma}e^{i\pi j/2}$ solves Eq. (2) (with $\theta = \pi$) for all j except at the edges ($j = 1, N$). As $\kappa \rightarrow \infty$, the system approaches this uniform state.

Just above the phase transition, the kink first appears at the right edge ($j = N$) – consistent with the fact that for $\theta = \pi$, the linear eigenstates in the vacuum phase are all localized at the right boundary. As κ increases further, the kink shifts toward the left boundary, leading to a continuous increase in the average amplitude $\langle r_j \rangle_j$ [Fig. 3(c)]. Numerically, we find that the kink position scales as $(\kappa - \kappa_{\text{crit}})^\beta$ with $\beta = -0.5$ near the phase transition [see inset in Fig. 3(c)]. This critical exponent can be understood as follows: nonreciprocity induces directional propagation toward the right (for $\theta = \pi$). This net current balances with the local pump and loss, saturating the right-most sites at an amplitude of $\sqrt{\kappa/\Gamma}$. Disregarding these saturated sites, the remaining sites with zero amplitude form an effective smaller system. The finite-size expression in Eq. (5) can then be used to determine the new, slightly larger κ required for the vacuum of this smaller system to become unstable. Alternatively, solving Eq. (5) for the effective system size – or equivalently the kink position – as a function of the distance from the phase transition $(\kappa - \kappa_{\text{crit}})$ yields precisely $\beta = -0.5$.

Next, we turn to the green region of the phase diagram in Fig. 3(a), which corresponds to time-dependent (dynamical) phases. This region has multiple attractors that encompasses a variety of phases and diverse dynamical behaviors. We will primarily focus on the most prominent of such phases, one that exists in almost the entire region. For fixed $\gamma/J < 1$, dynamical phases exist only within a finite range of κ : they transition to the vacuum phase at small κ and become unstable to the static condensate phase at large κ . To locate this upper phase boundary, we perform a numerical linear stability analysis of the static condensate state, yielding the red line in Fig. 3(a). Notably, the static condensate state α_j^s is \mathcal{PH} symmetric (i.e., $\mathcal{PH}[\alpha_j^s] = \alpha_j^s$).

Decreasing κ along the leftmost white dashed line in Fig. 3(a) towards the red line, the dynamical matrix describing fluctuations of the static condensate develops a second zero eigenvalue, whose eigenvector then coalesces with the Goldstone mode to yield an instability. We thus identify this portion of the red line as a second order CEP (see SM [54]). Below the red line of Fig. 3(a), the system spontaneously breaks the \mathcal{PH} symmetry, giving rise to two bistable time-dependent traveling wave states (wavevectors $q_\pm = q_s \pm \epsilon$) analogous to the PBC solutions in Eq. (4). The wavevectors q_\pm evolves continuously as κ is lowered, bifurcating from $q_\pm = q_s = \pi/2$ in the static phase (i.e. $\epsilon = 0$) to either $q_- = 0$ or $q_+ = \pi$

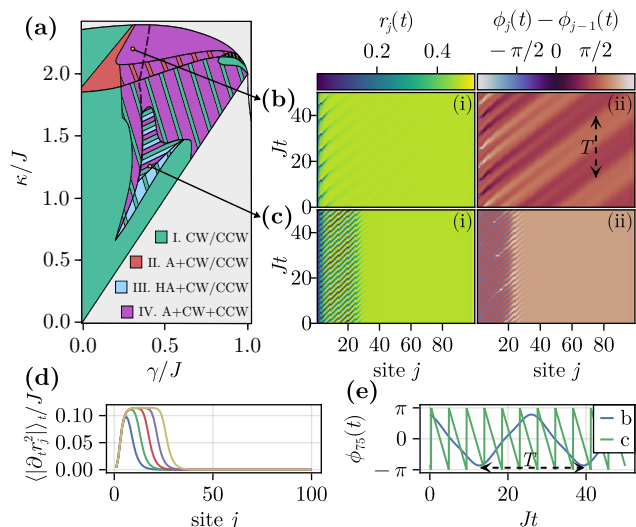


FIG. 4. (a) Zoom-in on the dynamical region of the steady-state OBC phase diagram from Fig. 3(a). Colored stripes indicate multistable regions with multiple phases with distinct dynamical phenomena. The dashed black line marks the approximate boundary where the bulk phase oscillations become chaotic (to the right of the line). (b, c) Space-time dynamics of the amplitude (i) and phase differences (ii) for representative points in phases IV and III at $\gamma = 0.3, \kappa = 2.2$ (b) and $\gamma = 0.4, \kappa = 1.25$ (c). (d) Time-averaged magnitude of the rate of change of the density in five different steady-states, corresponding to the parameters in (c). (e) Time-dependence of the phase of oscillator 75 corresponding to panels (b) and (c).

at the point where the system enters the vacuum phase (i.e. $\epsilon = \pi/2$). Similarly, as shown in Fig. 3(d), the frequency evolves continuously from zero, bifurcating into two branches corresponding to clockwise (CW) or counterclockwise (CCW) rotations (analogous to the “chiral” states in Ref. [8]). The \mathcal{PH} symmetry maps one solution onto the other, transforming a CW rotating state into a CCW one (i.e., flipping the sign of ω), while simultaneously flipping the wavevector from $q_s + \epsilon$ to $q_s - \epsilon$, and vice versa. Remarkably, the PBC result for the frequency in Eq. (3) holds perfectly for these two states, using the numerically extracted average wavevector $\langle q \rangle_j$.

Edge and bulk phase transitions. — So far, we have discussed cases where only the phase of each site was time-dependent. However, in some regions of parameter space within the dynamical phase, the amplitudes also becomes time-dependent. These amplitude fluctuations occur predominantly at the left edge of the system, resulting in distinct bulk versus edge behavior [see Fig. 4(a)]. In fact, the leftmost dashed-white line cut through the phase diagram of Fig. 3(a) already contains such an example. This is illustrated in Fig. 3(e), which displays the time- and space-averaged absolute value of the rate of change of the magnitude, $\langle |\partial_t r_j^2| \rangle_{j,t}$. This quantity is found to become nonzero at $\kappa/J \sim 1.9 - 2.2$. The inset in Fig. 3(e) shows

an example of the time-averaged spatial profile ($\langle |\partial_t r_j^2| \rangle_t$) of these amplitude fluctuations, revealing that they are peaked at the left edge. Away from the edge, this quantity quickly drops, and then exponentially decays into the bulk. Notably, these amplitude fluctuations do not affect the $\langle \omega \rangle_j$ order parameter shown in Fig. 3(d), as the dominant Fourier component, even for the left-most sites, remains at the same bulk value as the average value $\langle \omega \rangle_j$ depicted in Fig. 3(d).

The dynamical region ($\partial_t \alpha_j \neq 0$) in Fig. 4(a) includes additional phases with distinct edge and bulk behaviors, with some regions exhibiting multistability, as indicated by stripes in the phases in Fig. 4(a). Phase IV, indicated in purple in Fig. 4(a), features amplitude fluctuations at the left edge and phase-only oscillations in the bulk. A representative example (for $\gamma = 0.3, \kappa = 2.2$) of the amplitude and phase space-time dynamics is shown in Fig. 4(b,i) and Fig. 4(b,ii), respectively. Left of the black dashed line, the two limit cycles of phase I – the CW and the CCW solutions – merge, resulting in more complex behavior. The phases of the bulk sites act as pendula, involving both CW and CCW rotations [see Fig. 4(e)]. In some parts of this phase, particularly at smaller γ , the dynamics is nevertheless periodic. Notably, the \mathbb{Z}_2 symmetry is dynamically restored in this case, corresponding to \mathcal{PH} accompanied by the breaking of continuous time translation symmetry [58]. Specifically, the \mathcal{PH} operation acts as a translation by a half period, and the steady-state satisfies $\alpha_j(t) = \mathcal{PH}[\alpha_j(t + T/2)]$ for some period T (see SM [54] for details).

In Phase IV, the steady state alternates between exhibiting periodic and chaotic dynamics until a critical value of γ where only the chaotic dynamics persists. The transition occurs in the purple region to the right of the black dashed line in Fig. 4(a). Surprisingly, we find that despite the onset of chaos, the dynamics at the edge remain regular (see SM [54] for additional details). We also find a region [Phase III in Fig. 4(a)] with a hierarchy of steady states with varying edge lengths. A representative example ($\gamma = 0.4, \kappa = 1.25$) is shown in Fig. 4(c). The bulk dynamics is \mathcal{PH} broken, with CW or CCW phase oscillations [Fig. 4(e)] as in Phase I. We observe five steady states with progressively longer edge-amplitude fluctuations, shown in Fig. 4(d), although it remains unclear whether additional steady states exist. While the bulk dynamics in Phases II and III are periodic, the edge exhibits quasiperiodicity, breaking time translational symmetry and introducing an additional zero mode (beyond the existing Goldstone mode from a broken $U(1)$ symmetry, see SM [54]). Exploring these edge phase transitions in greater detail is left for future work.

Conclusions and outlook.—We have demonstrated how the NHSE and spatial nonreciprocity can fundamentally alter the phase diagram of driven-dissipative systems in a manner that strongly depends on boundary conditions. The remarkable differences between OBC and PBC seen

here are in stark contrast to the behavior of the fermionic and spin counterparts of our model [27, 48]. In those systems, excitations generically have a finite lifetime; they thus damp out before hitting the edge, making bulk properties insensitive to boundaries. In contrast, our bosonic system can possess an undamped zero mode (i.e. the Goldstone mode associated with the spontaneous $U(1)$ symmetry breaking). Such excitations can propagate to the boundaries, allowing a strong boundary-condition dependence.

Open boundary conditions, in our model, result in a particularly rich phase diagram, where even the condensation phase transition exhibits unconventional features compared to its reciprocal counterpart. This intriguing difference invites further exploration to understand whether they differ in their critical behavior. More broadly, the role of classical and quantum fluctuations beyond mean-field theory presents an exciting avenue for future research. Additionally, a deeper understanding of the observed edge phase transitions and their underlying mechanisms requires further investigation. Extending this work to higher dimensions [37] could uncover additional novel spatiotemporal patterns and exotic phases. Lastly, exploring the manifestation of these phenomena in active matter and other nonequilibrium systems remains an exciting direction for future studies.

Acknowledgments.— We acknowledge valuable discussions with M. Maghrebi, S. Diehl, J. Binysh, C. Coeuret. This work was supported by the Air Force Office of Scientific Research MURI program under Grant No. FA9550-19-1-0399, the Simons Foundation through a Simons Investigator award (Grant No. 669487), and was completed in part with resources provided by the University of Chicago’s Research Computing Center. RH was supported by Grant-in-Aid for Research Activity Start-up from JSPS in Japan (No. 23K19034). CW was partially supported by NSF-MPS-PHY award 2207383. This research benefited from Physics Frontier Center for Living Systems funded by the National Science Foundation (PHY- 2317138).

* ron.belyansky@gmail.com

- [1] L. M. Sieberer, M. Buchhold, J. Marino, and S. Diehl, Universality in driven open quantum matter, [arXiv:2312.03073](https://arxiv.org/abs/2312.03073).
- [2] I. Carusotto and C. Ciuti, Quantum fluids of light, *Rev. Mod. Phys.* **85**, 299 (2013).
- [3] F. Mivehvar, F. Piazza, T. Donner, and H. Ritsch, Cavity QED with quantum gases: New paradigms in many-body physics, *Adv. Phys.* **70**, 1 (2021).
- [4] T. Ozawa, H. M. Price, A. Amo, N. Goldman, M. Hafezi, L. Lu, M. C. Rechtsman, D. Schuster, J. Simon, O. Zeitlinger, and I. Carusotto, Topological photonics, *Rev. Mod. Phys.* **91**, 015006 (2019).
- [5] C. Noh and D. G. Angelakis, Quantum simulations and

- many-body physics with light, *Rep. Prog. Phys.* **80**, 016401 (2016).
- [6] A. Blais, A. L. Grimsmo, S. M. Girvin, and A. Wallraff, Circuit quantum electrodynamics, *Rev. Mod. Phys.* **93**, 025005 (2021).
- [7] Y. Avni, M. Fruchart, D. Martin, D. Seara, and V. Vitelli, The non-reciprocal Ising model, [arXiv:2311.05471](https://arxiv.org/abs/2311.05471).
- [8] M. Fruchart, R. Hanai, P. B. Littlewood, and V. Vitelli, Non-reciprocal phase transitions, *Nature* **592**, 363 (2021).
- [9] C. P. Zelle, R. Daviet, A. Rosch, and S. Diehl, Universal Phenomenology at Critical Exceptional Points of Nonequilibrium O (N) Models, *Phys. Rev. X* **14**, 021052 (2024).
- [10] Z.-F. Huang, M. te Vrugt, R. Wittkowski, and H. Löwen, Active pattern formation emergent from single-species nonreciprocity, [arXiv:2404.10093](https://arxiv.org/abs/2404.10093).
- [11] F. Brauns and M. C. Marchetti, Nonreciprocal Pattern Formation of Conserved Fields, *Phys. Rev. X* **14**, 021014 (2024).
- [12] Z. You, A. Baskaran, and M. C. Marchetti, Nonreciprocity as a generic route to traveling states, *Proc. Natl. Acad. Sci.* **117**, 19767 (2020).
- [13] S. Saha, J. Agudo-Canalejo, and R. Golestanian, Scalar Active Mixtures: The Nonreciprocal Cahn-Hilliard Model, *Phys. Rev. X* **10**, 041009 (2020).
- [14] R. Hanai, Nonreciprocal Frustration: Time Crystalline Order-by-Disorder Phenomenon and a Spin-Glass-like State, *Phys. Rev. X* **14**, 011029 (2024).
- [15] S. A. M. Loos, S. H. L. Klapp, and T. Martynek, Long-range order and directional defect propagation in the nonreciprocal XY model with vision cone interactions, *Phys. Rev. Lett.* **130**, 198301 (2023).
- [16] L. P. Dadhichi, J. Kethapelli, R. Chajwa, S. Ramaswamy, and A. Maitra, Nonmutual torques and the unimportance of motility for long-range order in two-dimensional flocks, *Phys. Rev. E* **101**, 052601 (2020).
- [17] G. Pisegna, S. Saha, and R. Golestanian, Emergent polar order in nonpolar mixtures with nonreciprocal interactions, *Proc. Natl. Acad. Sci.* **121**, e2407705121 (2024).
- [18] A. Murugan and S. Vaikuntanathan, Topologically protected modes in non-equilibrium stochastic systems, *Nat Commun.* **8**, 13881 (2017).
- [19] L. Parkavousi, N. Rana, R. Golestanian, and S. Saha, Enhanced stability and chaotic condensates in multi-species non-reciprocal mixtures, [arXiv:2408.06242](https://arxiv.org/abs/2408.06242).
- [20] M. J. Bowick, N. Fakhri, M. C. Marchetti, and S. Ramaswamy, Symmetry, Thermodynamics, and Topology in Active Matter, *Phys. Rev. X* **12**, 010501 (2022).
- [21] C. Zheng and E. Tang, A topological mechanism for robust and efficient global oscillations in biological networks, *Nat Commun* **15**, 6453 (2024).
- [22] H. Sompolinsky and I. Kanter, Temporal Association in Asymmetric Neural Networks, *Phys. Rev. Lett* **57**, 2861 (1986).
- [23] R. Khasseh, S. Wald, R. Moessner, C. A. Weber, and M. Heyl, Active quantum flocks, [arXiv:2308.01603](https://arxiv.org/abs/2308.01603).
- [24] T. Nadolny, C. Bruder, and M. Brunelli, Nonreciprocal Synchronization of Active Quantum Spins, *Phys. Rev. X* **15**, 011010 (2025).
- [25] E. I. R. Chiacchio, A. Nunnenkamp, and M. Brunelli, Nonreciprocal Dicke Model, *Phys. Rev. Lett.* **131**, 113602 (2023).
- [26] R. Hanai, D. Ootsuki, and R. Tazai, Photoinduced non-reciprocal magnetism, [arXiv:2406.059572](https://arxiv.org/abs/2406.059572).
- [27] S. E. Begg and R. Hanai, Quantum Criticality in Open Quantum Spin Chains with Nonreciprocity, *Phys. Rev. Lett.* **132**, 120401 (2024).
- [28] N. Hatano and D. R. Nelson, Vortex pinning and non-Hermitian quantum mechanics, *Phys. Rev. B* **56**, 8651 (1997).
- [29] N. Hatano and D. R. Nelson, Localization Transitions in Non-Hermitian Quantum Mechanics, *Phys. Rev. Lett.* **77**, 570 (1996).
- [30] S. Yao and Z. Wang, Edge States and Topological Invariants of Non-Hermitian Systems, *Phys. Rev. Lett.* **121**, 086803 (2018).
- [31] X. Zhang, T. Zhang, M.-H. Lu, and Y.-F. Chen, A review on non-Hermitian skin effect, *Adv. Phys. X* **7**, 2109431 (2022).
- [32] N. Okuma and M. Sato, Non-Hermitian Topological Phenomena: A Review, *Annu. Rev. Condens. Matter Phys.* **14**, 83 (2023).
- [33] S. Ghosh, K. Sengupta, and I. Paul, Hilbert space fragmentation imposed real spectrum of non-Hermitian systems, *Phys. Rev. B* **109**, 045145 (2024).
- [34] B. Many Manda, R. Carretero-González, P. G. Kevrekidis, and V. Achilleos, Skin modes in a nonlinear Hatano-Nelson model, *Phys. Rev. B* **109**, 094308 (2024).
- [35] S.-B. Zhang, M. M. Denner, T. Bzdušek, M. A. Sentef, and T. Neupert, Symmetry breaking and spectral structure of the interacting Hatano-Nelson model, *Phys. Rev. B* **106**, L121102 (2022).
- [36] M. Ezawa, Dynamical nonlinear higher-order non-Hermitian skin effects and topological trap-skin phase, *Phys. Rev. B* **105**, 125421 (2022).
- [37] B. Zhu, Q. Wang, D. Leykam, H. Xue, Q. J. Wang, and Y. D. Chong, Anomalous Single-Mode Lasing Induced by Nonlinearity and the Non-Hermitian Skin Effect, *Phys. Rev. Lett.* **129**, 013903 (2022).
- [38] P. Brighi and A. Nunnenkamp, Nonreciprocal dynamics and the non-hermitian skin effect of repulsively bound pairs, *Phys. Rev. A* **110**, L020201 (2024).
- [39] J. Veenstra, O. Gamayun, X. Guo, A. Sarvi, C. V. Meinersen, and C. Coulais, Non-reciprocal topological solitons in active metamaterials, *Nature* **627**, 528 (2024).
- [40] R. Hanai, A. Edelman, Y. Ohashi, and P. B. Littlewood, Non-hermitian phase transition from a polariton bose-einstein condensate to a photon laser, *Phys. Rev. Lett.* **122**, 185301 (2019).
- [41] R. Hanai and P. B. Littlewood, Critical fluctuations at a many-body exceptional point, *Phys. Rev. Res.* **2**, 033018 (2020).
- [42] T. Suchanek, K. Kroy, and S. A. M. Loos, Irreversible mesoscale fluctuations herald the emergence of dynamical phases, *Phys. Rev. Lett.* **131**, 258302 (2023).
- [43] Y. Nakanishi, R. Hanai, and T. Sasamoto, Continuous time crystals as a pt symmetric state and the emergence of critical exceptional points (2024), [arXiv:2406.09018](https://arxiv.org/abs/2406.09018).
- [44] C. Weis, M. Fruchart, R. Hanai, K. Kawagoe, P. B. Littlewood, and V. Vitelli, Exceptional points in nonlinear and stochastic dynamics, [arXiv:2207.11667](https://arxiv.org/abs/2207.11667).
- [45] H.-P. Breuer and F. Petruccione, *The Theory of Open Quantum Systems*, repr ed. (Clarendon Press, Oxford, 2010).
- [46] A. Metelmann and H. E. Türeci, Nonreciprocal signal routing in an active quantum network, *Phys. Rev. A* **97**,

- 043833 (2018).
- [47] C. C. Wanjura, M. Brunelli, and A. Nunnenkamp, Topological framework for directional amplification in driven-dissipative cavity arrays, *Nat Commun* **11**, 3149 (2020).
- [48] A. McDonald, R. Hanai, and A. A. Clerk, Nonequilibrium stationary states of quantum non-Hermitian lattice models, *Phys. Rev. B* **105**, 064302 (2022).
- [49] L. He, L. M. Sieberer, E. Altman, and S. Diehl, Scaling properties of one-dimensional driven-dissipative condensates, *Phys. Rev. B* **92**, 155307 (2015).
- [50] J. Marino and S. Diehl, Driven Markovian Quantum Criticality, *Phys. Rev. Lett.* **116**, 070407 (2016).
- [51] L. He, L. M. Sieberer, and S. Diehl, Space-Time Vortex Driven Crossover and Vortex Turbulence Phase Transition in One-Dimensional Driven Open Condensates, *Phys. Rev. Lett.* **118**, 085301 (2017).
- [52] F. Vercesi, Q. Fontaine, S. Ravets, J. Bloch, M. Richard, L. Canet, and A. Minguzzi, Phase diagram of one-dimensional driven-dissipative exciton-polariton condensates, *Phys. Rev. Res.* **5**, 043062 (2023).
- [53] Q. Fontaine, D. Squizzato, F. Baboux, I. Amelio, A. Lemaitre, M. Morassi, I. Sagnes, L. Le Gratiet, A. Harouri, M. Wouters, I. Carusotto, A. Amo, M. Richard, A. Minguzzi, L. Canet, *et al.*, Kardar-Parisi-Zhang universality in a one-dimensional polariton condensate, *Nature* **608**, 687 (2022).
- [54] See Supplemental Material for additional details concerning the stability of the PBC solutions, the spectrum of Hatano-Nelson model, and additional details concerning the dynamical phases for OBC. Includes Refs. [59–61].
- [55] I. S. Aranson and L. Kramer, The world of the complex Ginzburg-Landau equation, *Rev. Mod. Phys.* **74**, 99 (2002).
- [56] J. F. Ravoux, S. Le Dizès, and P. Le Gal, Stability analysis of plane wave solutions of the discrete Ginzburg-Landau equation, *Phys. Rev. E* **61**, 390 (2000).
- [57] K. Kawabata, K. Shiozaki, M. Ueda, and M. Sato, Symmetry and Topology in Non-Hermitian Physics, *Phys. Rev. X* **9**, 041015 (2019).
- [58] V. Khemani, R. Moessner, and S. L. Sondhi, A Brief History of Time Crystals, (2019), [arXiv:1910.10745](https://arxiv.org/abs/1910.10745).
- [59] O. E. Rössler, The chaotic hierarchy, in *A Chaotic Hierarchy* (WORLD SCIENTIFIC, 1991) pp. 25–47.
- [60] O. E. Rossler, An equation for hyperchaos, *Physics Letters A* **71**, 155 (1979).
- [61] G. Benettin, L. Galgani, A. Giorgilli, and J.-M. Strelcyn, Lyapunov Characteristic Exponents for smooth dynamical systems and for hamiltonian systems; A method for computing all of them. Part 2: Numerical application, *Meccanica* **15**, 21 (1980).

Supplemental Material for: Phase Transitions in Nonreciprocal Driven-Dissipative Condensates

Ron Belyansky,¹ Cheyne Weis,² Ryo Hanai,³ Peter B. Littlewood,^{2,4} and Aashish A. Clerk¹

¹*Pritzker School of Molecular Engineering, University of Chicago, Chicago, IL 60637, USA*

²*James Franck Institute and Department of Physics, The University of Chicago, Chicago, Illinois 60637, United States*

³*Department of Physics, Institute of Science Tokyo, 2-12-1 Ookayama Meguro-ku, Tokyo, 152-8551, Japan*

⁴*School of Physics and Astronomy, University of St Andrews, N Haugh, St Andrews KY16 9SS, United Kingdom*

(Dated: February 11, 2025)

This Supplemental Material is organized as follows. In Sec. I, we derive the stability condition of the condensate solutions for the PBC system. In Sec. II, we derive the spectrum of the OBC Hatano-Nelson, including Eq. (5) of the main text. In Sec. III, we provide additional details on the phases and phases transitions in the OBC system. In particular, in Sec. III A we demonstrate the existence of critical exceptional points; in Sec. III B we discuss the Lyapunov spectrum in each of the dynamics phases and demonstrate the existence of quasiperiodicity and chaos; in Sec. III C, we numerically validate the \mathbb{Z}_2 symmetry restoration occurring in Phase IV and discuss the bulk properties of the chaotic dynamics; in Sec. III D, we discuss the edge dynamics throughout the dynamic portion of the phase diagram.

I. PERIODIC BOUNDARY CONDITIONS

In this section, we derive the stability condition of the PBC solutions from Eq. (4) of the main text that lead to the plot shown in Fig. 2 of the main text.

The momentum- q condensate solution for PBC is given by

$$\alpha_j(t) = r_q e^{iqj - i\omega_q t}, \quad r_q = \sqrt{\frac{\kappa - \gamma_q}{\Gamma}}, \quad \gamma_q = 2\gamma(1 + \sin(q + \theta)), \quad \omega_q = -2J \cos(q), \quad (\text{S1})$$

for all $q = 2\pi m/N$, $m = 0, \dots, N-1$ satisfying $\kappa - \gamma_q > 0$.

We consider momentum-space fluctuations on top of the momentum- q condensate of the form

$$\alpha_j(t) = r_q e^{-i\omega_q t + iqj} + e^{-i\omega_q t} \sum_k e^{ikj} \delta\alpha_k. \quad (\text{S2})$$

To first order in $\delta\alpha_k$, we get

$$\partial_t \delta\alpha_k = (\kappa - \gamma_k - 2\Gamma r_q^2 - i(\omega_k - \omega_q)) \delta\alpha_k - \Gamma r_q^2 \delta\alpha_{2q-k}^* \equiv \beta_k \delta\alpha_k - \Lambda \delta\alpha_{2q-k}^*. \quad (\text{S3})$$

The stability of the momentum- q condensate is then determined by the eigenvalues of

$$\partial_t \begin{pmatrix} \delta\alpha_k \\ \delta\alpha_{2q-k}^* \end{pmatrix} = \begin{pmatrix} \beta_k & -\Lambda \\ -\Lambda & \beta_{2q-k}^* \end{pmatrix} \begin{pmatrix} \delta\alpha_k \\ \delta\alpha_{2q-k}^* \end{pmatrix}. \quad (\text{S4})$$

The eigenvalues are given by

$$\lambda_{k,\pm} = \frac{\beta_k + \beta_{2q-k}^*}{2} \pm \frac{1}{2} \sqrt{(\beta_k - \beta_{2q-k}^*)^2 + \Lambda^2}. \quad (\text{S5})$$

The momentum- q traveling wave is stable if

$$\max_k [\text{Re}(\lambda_{k,+})] < 0. \quad (\text{S6})$$

We evaluate Eq. (S6) numerically to produce Fig. 2 of the main text. While a full analytical expression for Eq. (S6) is too cumbersome, we can obtain a simple result in the limit of $\kappa \rightarrow \infty$. In that case, we obtain $\lambda_{k,+} = -2\gamma(\cos(k) - 1)\sin(q + \theta)$. The stability condition in this limit thus becomes

$$\sin(q + \theta) < 0. \quad (\text{S7})$$

For $\theta = \pi$, we see that only right-moving modes, $0 < q < \pi$, are stable as $\kappa \rightarrow \infty$, consistent with the numerical results in Fig. 2 of the main text.

II. HATANO-NELSON

In this section, we derive the spectrum of the OBC Hatano-Nelson, shown in Eq. (5) of the main text. The Hatano-Nelson Hamiltonian [Eq. (1) of the main text] is

$$H_{\text{HN}} = \begin{pmatrix} \Delta & J_+ & & & \\ J_- & \Delta & J_+ & & \\ & J_- & \ddots & \ddots & \\ & & & \ddots & \ddots \\ & & & & \ddots & \ddots \end{pmatrix}. \quad (\text{S8})$$

The eigenvalue equation, $H_{\text{HN}}\psi = \lambda\psi$ yields to the bulk equations:

$$J_- \psi_{j-1} + E\psi_j + J_+ \psi_{j+1} = 0, \quad 1 < j < N, \quad (\text{S9})$$

where $E \equiv \Delta - \lambda$. For the boundaries, we have instead

$$E\psi_1 + J_+ \psi_2 = 0, \quad (\text{S10})$$

$$J_- \psi_{N-1} + E\psi_N = 0. \quad (\text{S11})$$

The bulk equation Eq. (S9) is solved with the eigenvector $\psi(z) = (z, z^2, \dots, z^N)^T$ giving

$$J_- + Ez + J_+ z^2 = 0. \quad (\text{S12})$$

For a given E , Eq. (S12) is a quadratic equation that has two solutions z_1, z_2 . Hence the general solution is a superposition $\Psi = c_1\psi(z_1) + c_2\psi(z_2)$. Plugging this into the boundaries equations Eq. (S10) gives

$$H_B \begin{pmatrix} c_1 \\ c_2 \end{pmatrix} = 0 \quad \text{where} \quad H_B = \begin{pmatrix} Ez_1 + J_+ z_1^2 & Ez_2 + J_+ z_2^2 \\ J_- z_1^{N-1} + Ez_1^N & J_- z_2^{N-1} + Ez_2^N \end{pmatrix}. \quad (\text{S13})$$

H_B has a nontrivial nullspace iff $\det(H_B) = 0$, implying (assuming $J_- \neq 0$)

$$-z_1^{N+1} + z_2^{N+1} = 0 \quad \text{and} \quad c_1 = -c_2. \quad (\text{S14})$$

For $J_- \neq 0$, Eq. (S12) implies

$$z_1 z_2 = \frac{J_-}{J_+}, \quad (\text{S15})$$

which we can solve by

$$z_1 = r e^{i\theta} e^{i\delta/2}, \quad z_2 = r e^{-i\theta} e^{i\delta/2} \quad \text{where} \quad r^2 = \left| \frac{J_-}{J_+} \right| \quad \text{and} \quad \arg\left(\frac{J_-}{J_+}\right) = \delta. \quad (\text{S16})$$

Plugging this into Eq. (S14) yields

$$r^{N+1} \sin(\theta(N+1)) = 0 \rightarrow \theta_m = \frac{\pi m}{N+1}, \quad m = 1, \dots, N. \quad (\text{S17})$$

Equation (S12) then gives the eigenvalues

$$\lambda_m = \Delta + 2e^{-i\delta/2} J_- \sqrt{\left| \frac{J_+}{J_-} \right|} \cos(\theta_m), \quad (\text{S18})$$

and the corresponding eigenvectors are

$$\Psi_m = (r e^{i\delta/2} \sin(\theta_m), r^2 e^{i\delta} \sin(2\theta_m), \dots, r^N e^{i\delta N/2} \sin(\theta_m N))^T. \quad (\text{S19})$$

III. OPEN BOUNDARY CONDITIONS

In this section, we provide further details on the phase transitions and phenomena that occur for the open boundary conditions. There are three explicit symmetries that occur in the model and can be broken in the bulk, or in some cases purely on the edge of the chain. For all values of θ , the EOM, Eq. (2) of the main text, admit a $U(1) \cong SO(2)$ symmetry and a time translational symmetry. As discussed in the text, the particle-hole operator is defined as $\mathcal{PH}[\alpha_j] = e^{i\pi j} \alpha_j^*(t)$, which is an involutory operator ($\mathcal{PH}^2 = \mathbb{I}$). Applying the \mathcal{PH} to Eq. (2) of the main text yields

$$i\partial_t \alpha_j^* = i(\kappa - 2\gamma)\alpha_j^* - i\Gamma|\alpha_j|^2\alpha_j^* + (J + \gamma e^{-i\theta})\alpha_{j+1}^* + (J - \gamma e^{-i\theta})\alpha_{j-1}^*. \quad (\text{S20})$$

When $\theta = 0, \pi$, $\mathcal{PH}[\alpha_j]$ follows identical equation of motion as α_j , resulting in a \mathbb{Z}_2 symmetry via application of the \mathcal{PH} operator. The full symmetry group for $\theta = 0, \pi$ becomes $O(2) \cong SO(2) \times \mathbb{Z}_2$ allowing for the richer phase diagram and collective phenomena. As in the main text, we exclusively consider the \mathcal{PH} -symmetric cases of $\theta = 0, \pi$, choosing $\theta = \pi$ for concreteness.

A. \mathcal{PH} -symmetry breaking and critical exceptional points

In the static phase, the solutions takes the form $\alpha_j = r_j e^{i(\phi + \pi j/2)}$ for some value of ϕ (due to spontaneous breaking of $U(1)$). \mathcal{PH} is left unbroken as $\alpha_j \sim \mathcal{PH}[\alpha_j]$, where we use \sim to mean equivalent for some global rotation by an element of $U(1)$. In Phase I, the long time behavior admits two families of possible solutions of the form $\alpha_j^\pm = r_j e^{i(\pm\omega t + iq_\pm j + \phi)}$, where $q_\pm = \pi/2 \pm \epsilon$. Note that $\mathcal{PH}[\alpha_j^\pm] \sim \alpha_j^\mp$ implying that \mathcal{PH} -symmetry is broken because there does not exist a $U(1)$ transformation such that $\mathcal{PH}[\alpha_j^\pm]$ and α_j^\pm become equal at all times.

Transitions between static and dynamic \mathbb{Z}_2 -symmetry broken phases have been previously shown to occur at a critical exceptional points (CEP), a critical point that has multiple zero modes with the corresponding eigenvectors aligned [S1–S4]. A critical exceptional line exists on the red line in Fig. 3(a) of the main text, excluding the portion forming the border between the static phase and Phase IV as shown at $\gamma = 0.4$ in Fig. S1. We numerically demonstrate the CEP in Fig. S1 for values of γ which approach Phase I (i.e., $\gamma = \{0.1, 0.2, 0.3\}$). The dynamical matrix (i.e. the Jacobian of the equations of motion, defined as $J_{ij} = \frac{\partial \dot{\alpha}_i}{\partial \alpha_j}$ with i and j indexing both the sites and their complex conjugates) is evaluated on the steady state solution for values of κ approaching the dynamical region from the static phase. At $\kappa = \kappa_c$, the Jacobian exhibits a 2nd order exceptional point, where the mode undergoing critical slowing aligns with the existing Goldstone mode from $U(1)$ symmetry breaking. We expect the transition to be an exceptional point when approached from the limit cycle phase as well, as found in previous works [S2, S3].

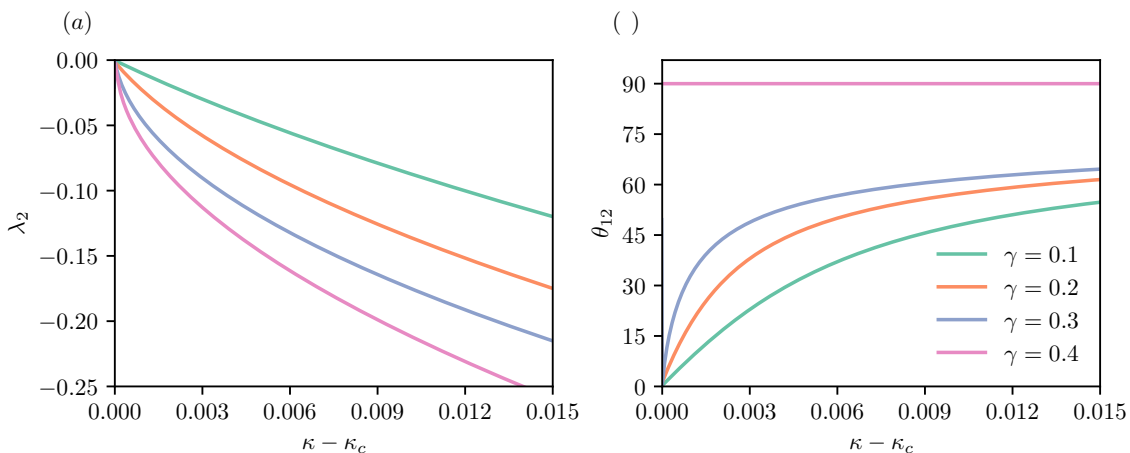


FIG. S1. Demonstration of the critical exceptional point (CEP) between the vacuum and Phase I. (a) The second largest eigenvalue λ_2 of the Jacobian as a function of the distance from the critical point $\kappa - \kappa_c$. (b) The angle between the first two eigenvectors θ_{12} of the Jacobian. The critical values for $\gamma = \{0.1, 0.2, 0.3, 0.4\}$ are respectively $\kappa_c \approx \{2.3734, 2.3848, 2.3893, 2.3935\}$.

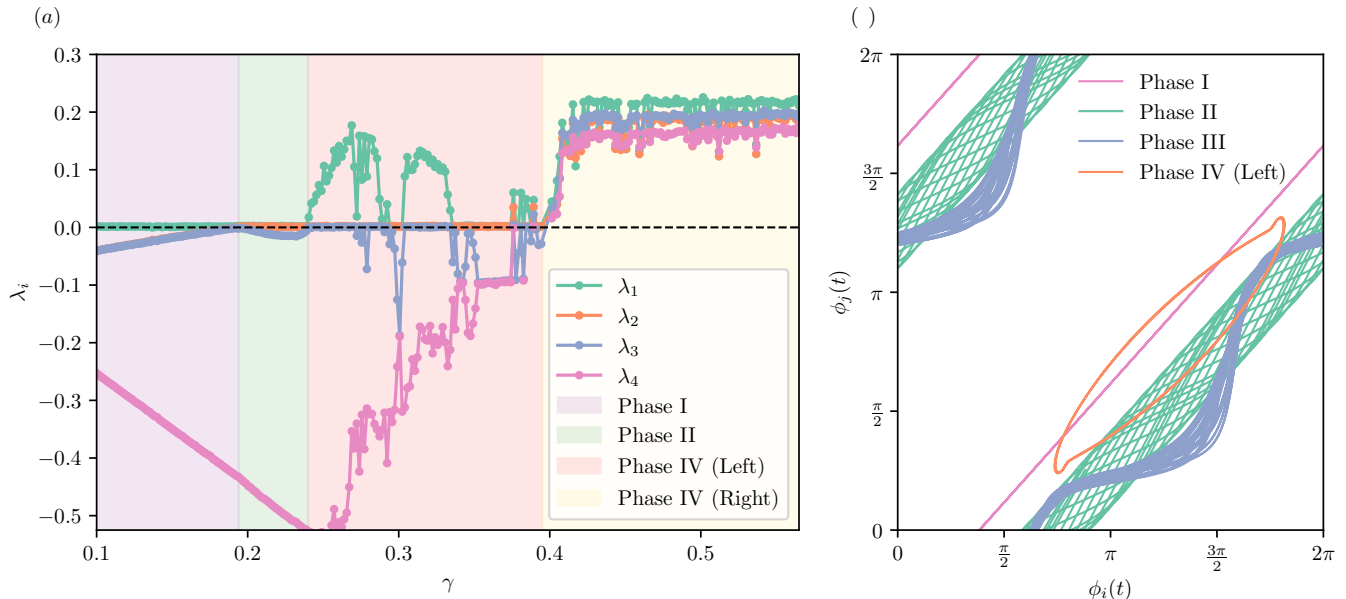


FIG. S2. (a) Sweep of the 4 largest Lyapunov characteristic exponents at $\kappa = 2.2$ and $N = 100$. Phase IV (Left) and (Right) refer to the portion of Phase IV on the corresponding side of the dotted black line in Fig. 4(a) of the main text. (b) A phase space plot of $\phi_j(t) := \arg(\alpha_j(t))$ for two sites near the edge of the chain with the Phase I trajectory at $\kappa = 2.2$, $\gamma = 0.1$ with $i = 1, j = 2$, Phase II at $\kappa = 2$, $\gamma = 0.2$ with $i = 1, j = 2$, Phase III at $\kappa = 1.25$, $\gamma = 0.4$ with $i = 11, j = 12$, and Phase IV at $\kappa = 2.2$, $\gamma = 0.35$ with $i = 11, j = 12$.

B. Lyapunov spectrum of the dynamical phases

In this section, we demonstrate features of the other various dynamical phases by numerically computing their associated Lyapunov characteristic exponents (LCEs). In Fig. S2(a), we plot the four largest LCEs for a horizontal cut through the phase diagram of Fig. 4(a) of the main text for a fixed $\kappa = 2.2$. We compute the LCEs using an implementation of the Benettin et al. algorithm [S5], which time evolves the tangent space vectors and extracts Lyapunov exponents from the logarithmic growth or decay of the scaling factors coming from a QR decomposition. We divide Phase IV into two parts (left and right), depending on whether the value of γ is to the left or right of the dashed line in Fig. 4(a). While in Phase I there is a single zero mode (associated with the breaking of $U(1)$ symmetry), the onset of edge amplitude dynamics in Phase II and Phase IV (Left) coincides with the existence of two zero modes. Phase III, although not shown in Fig. S2(a), also admits two zero modes. Generically, the existence of multiple zero modes corresponds to quasiperiodic dynamics, due to the modes oscillating at incommensurate frequencies. This non-repeating dynamics is observed in the trajectories in Phases II and III in two sites near the left edge in Fig. S2, whereas periodic motion is retained in Phase I and IV (Left). In both phases, quasiperiodicity is localized towards the left edge of the chain (where both the phases and amplitudes are time-dependent). The edge dynamics in Phases II and III are analogous to the dynamics of the “chiral+swap” phase in [S3].

The portion of Phase IV (Left) plotted is uni-stable, but admits intermittent chaos throughout the phase, i.e. the dynamics is chaotic for values of γ where a single LCE becomes positive. Phase IV (Right) generically admits multiple positive Lyapunov exponents, known in dynamical systems as hyperchaos [S6, S7], implying that this phase admits a higher dimensional chaotic attractor than the intermittent chaos seen in Phase IV (Left).

C. \mathcal{PH} -symmetry restoration

In the nonchaotic portion of Phase IV (Left), the system retains periodicity in spite of the existence of two zero modes. The time derivative of the total phase coordinate, $\dot{\Phi} = (1/N) \sum \dot{\phi}_i$, averages to zero in this phase, in contrast to \mathcal{PH} -broken Phase I where $\dot{\Phi} = \pm\omega$. The discrete time translation symmetry is restored because the Goldstone mode associated with Φ is now at zero frequency, making the zero modes commensurate. A \mathbb{Z}_2 symmetry restoration also takes place, taking the explicit form $\alpha_j(t) \sim \mathcal{PH}[\alpha_j(t + T/2)]$. In Fig. S3, we demonstrate the symmetry restoration

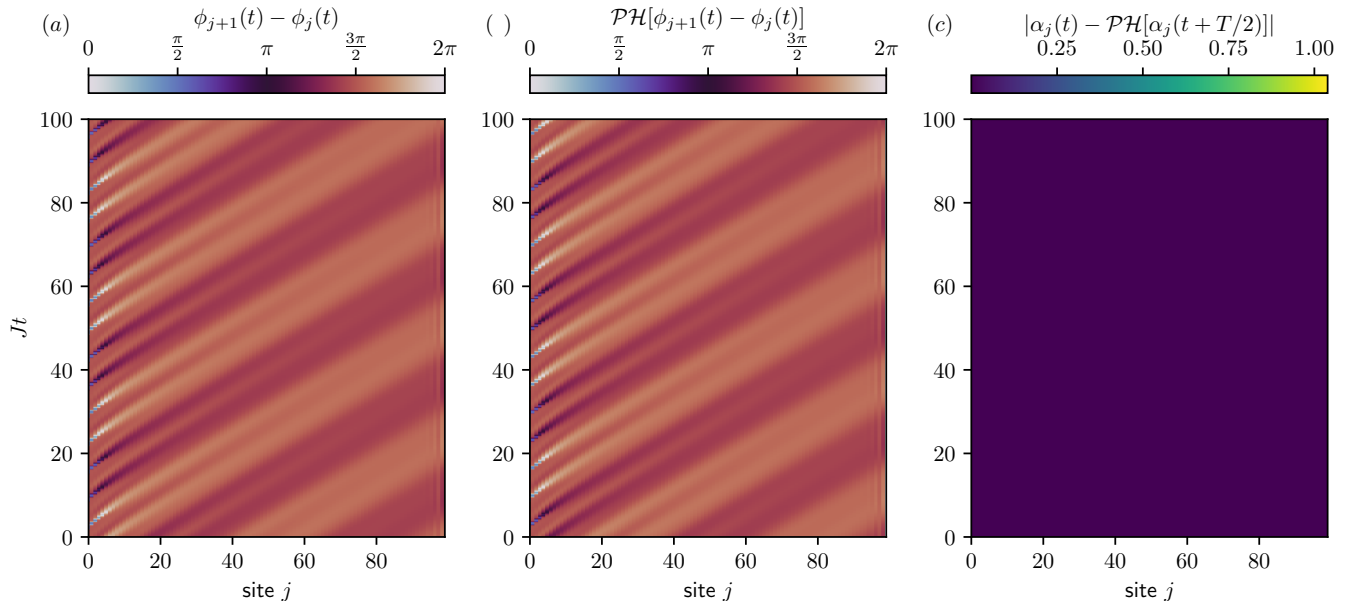


FIG. S3. A demonstration of the \mathcal{PH} restoration at $\kappa = 2.2, \gamma = 0.3$, corresponding to point (b) in Fig. 4(a) of the main text. (a) Space-time dynamics of the phase differences, $\phi_{j+1}(t) - \phi_j(t)$. (b) Space-time dynamics of the phase differences of the \mathcal{PH} -conjugated solution. Specifically, $\mathcal{PH}[\phi_{j+1}(t) - \phi_j(t)] := \arg(\mathcal{PH}[\alpha_{j+1}(t)]) - \arg(\mathcal{PH}[\alpha_j(t)])$. (c) The magnitude of $\alpha_j(t) - \mathcal{PH}[\alpha_j(t + T/2)]$, where $T \approx 26.66$ for this choice of parameters. For numerical convenience, the arbitrary global phase of $\alpha_j(t)$ is chosen such that no additional rotation is needed for $\alpha_j(t) - \mathcal{PH}[\alpha_j(t + T/2)]$ to be zero.

at a periodic point of Phase IV (Left), showing the symmetry persists to the edge where atypical amplitude dynamics occur. In Fig. S3(b), the \mathcal{PH} -conjugate solution can clearly be seen as a time translation of the original solution. As the \mathbb{Z}_2 symmetry operation is an involution, this time translation can only be a half of the period of the solution. The difference between the original and the time shifted \mathcal{PH} -conjugate solution is shown to be within numerical error of zero in Fig. S3(c).

In the chaotic/hyperchaotic portions of Phase IV, time translation symmetry is completely broken, meaning that no subgroup of continuous time translations are preserved by the steady state dynamics. The system exhibits domains of clockwise (CW) and counterclockwise (CCW) rotation corresponding to the two colors of stripes in Fig. S4(a). Intermittent switching between directions of rotation leads to the diffusion of the phase variables for sites further from the edge. The trajectory exhibits no net preference for CW or CCW motion at long times, as illustrated in Fig. S4(b). The various phases trajectories remain centered near zero at each point in time, resembling an unbiased random walk.

In the periodic portion of Phase IV, the \mathbb{Z}_2 symmetry restoration $\alpha_j(t) \sim \mathcal{PH}[\alpha_j(t + T/2)]$ implies that the \mathcal{PH} operation maps the entirety of the limit cycle trajectory back onto itself. This symmetry appears to be retained as the periodic orbit bifurcates into the chaotic attractor, such that the set of points on the chaotic attractor is now invariant under the \mathcal{PH} operation as we demonstrate in Fig. S4(c-d). In (c), we use a delay coordinate representation to give a low dimensional projection of the chaotic attractor. The attractor generated by the \mathcal{PH} conjugated initial condition, shown in (d), is nearly identical to the original attractor, up to small deviations due to only plotting a finite sample of the attractor. This implies that the chaotic attractor admits a \mathbb{Z}_2 symmetry despite the complete lack of periodicity. We leave to future work the further verification of symmetry restoration on the chaotic attractor and the study of its implications.

We have now explored how each symmetry is expressed in all of the OBC phases found in this work. We summarize this discussion with Table S1 listing the action of the three symmetries in each phase.

D. Edge dynamics

To conclude, we explore the irregular dynamics that can occur at the edge of the chain. One example was already demonstrated in Fig. S2(a) at the phase transition occurring at the boundary of Phase I and II. The bulk dynamics

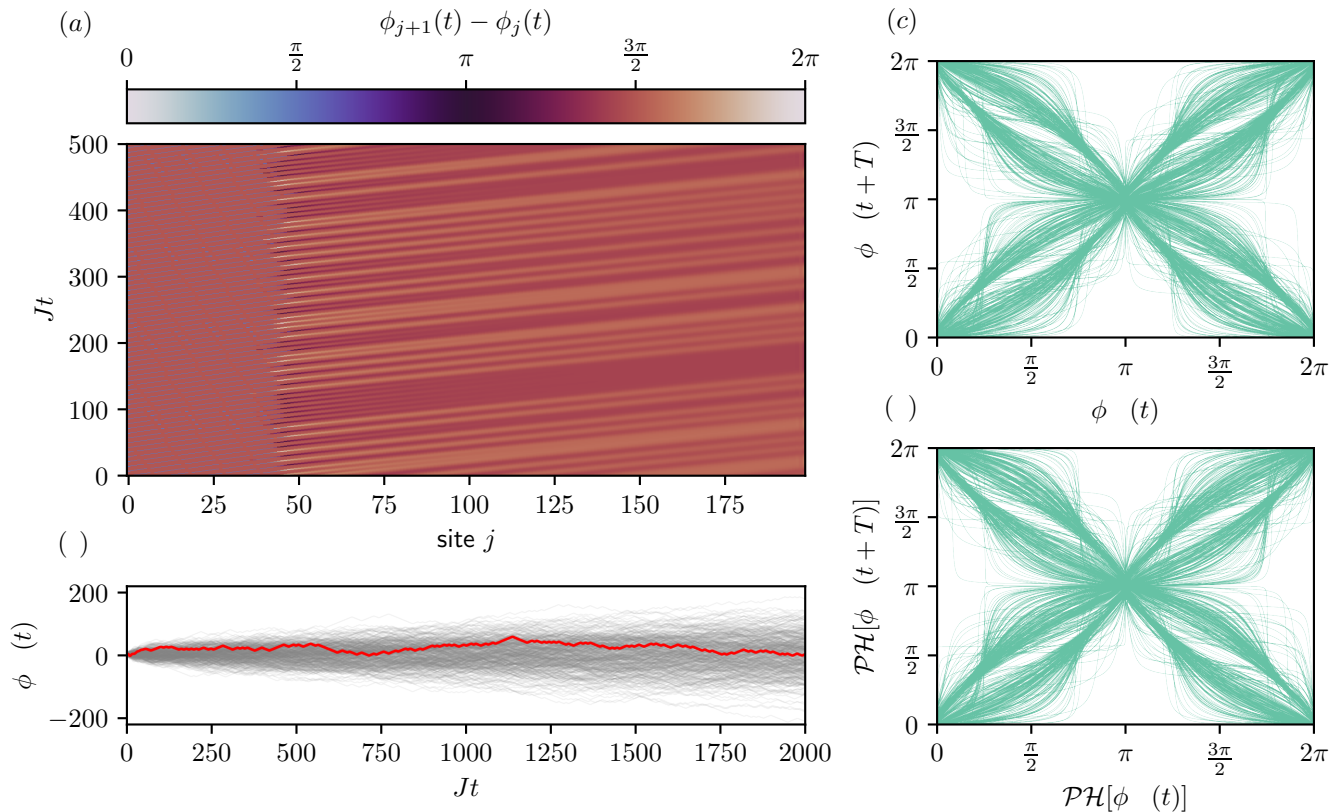


FIG. S4. (a) Time and space behavior of adjacent phase differences for $\kappa = 2.2$, $\gamma = 0.5$, demonstrating chaotic dynamics. (b) Temporal behavior of the phase for a site in the bulk ($j = 85$), for 300 nearby trajectories on the chaotic attractor with an example trajectory highlighted in red. (c-d) Plots a time delay embedding of the chaotic attractor, formed by looking at the behavior of the phase on site $j = 50$ at both times t and $t + T$, for a fixed delay time $T = 14/J$. We also plot the \mathcal{PH} conjugate attractor, where $\mathcal{PH}[\phi_j(t)] := \arg(\mathcal{PH}[\alpha_j(t)])$. The choice of T is comparable to the return time for each site.

on either side of this transition are identical, but the left edge exhibits quasiperiodic behavior in Phase II, and critical slowing down (i.e., a 3rd zero mode) at the boundary between the two phases. The dynamics in Phase II is shown in Fig. S5(a), where the nonuniform phase oscillations decay into the bulk [similar to the decay of the amplitude fluctuations shown in the inset of Fig. 3(e) of the main text]. Phase III is similarly only distinguished from Phase I by amplitude and additional phase oscillations occurring near the edge. A hierarchy of these steady state solutions exist, as demonstrated in Fig. 4(d) of the main text. The quantized length scale distinguishing consecutive edge modes can be found for this choice of parameters via integration of the curves in Fig. 4(d), of which the mean difference is ~ 4.2 sites, roughly half the wavelength of the bulk phase oscillations, ~ 8.2 sites.

Phase IV (Right), the hyperchaotic phase, displays distinct edge dynamics compared to Phase IV (Left). The first ~ 40 sites of the chain predominantly exhibit amplitude dynamics. Domain walls separating regions of $\phi = 0$ and

Phase	$U(1)$	\mathbb{Z}_2	Continuous Time Translation
Vacuum	Unbroken	Unbroken	Unbroken
Static	Broken	Unbroken	Unbroken
Dynamic Phase I	Broken	Broken	Broken to Discrete Translations
Dynamic Phase II, III	Broken	Broken	Broken ^a
Dynamic Phase IV (periodic)	Broken	Dynamically Restored	Broken to Discrete Translations
Dynamic Phase IV (chaotic)	Broken	Restored on Attractor	Completely Broken

^a Phases II and III exhibit quasiperiodicity, particularly near the edge of the chain. Certain choices of measurements will admit a discrete time translational symmetry for quasiperiodic steady states, although the dynamics of the total state never repeat in time.

TABLE S1. Symmetry actions for each OBC phase.

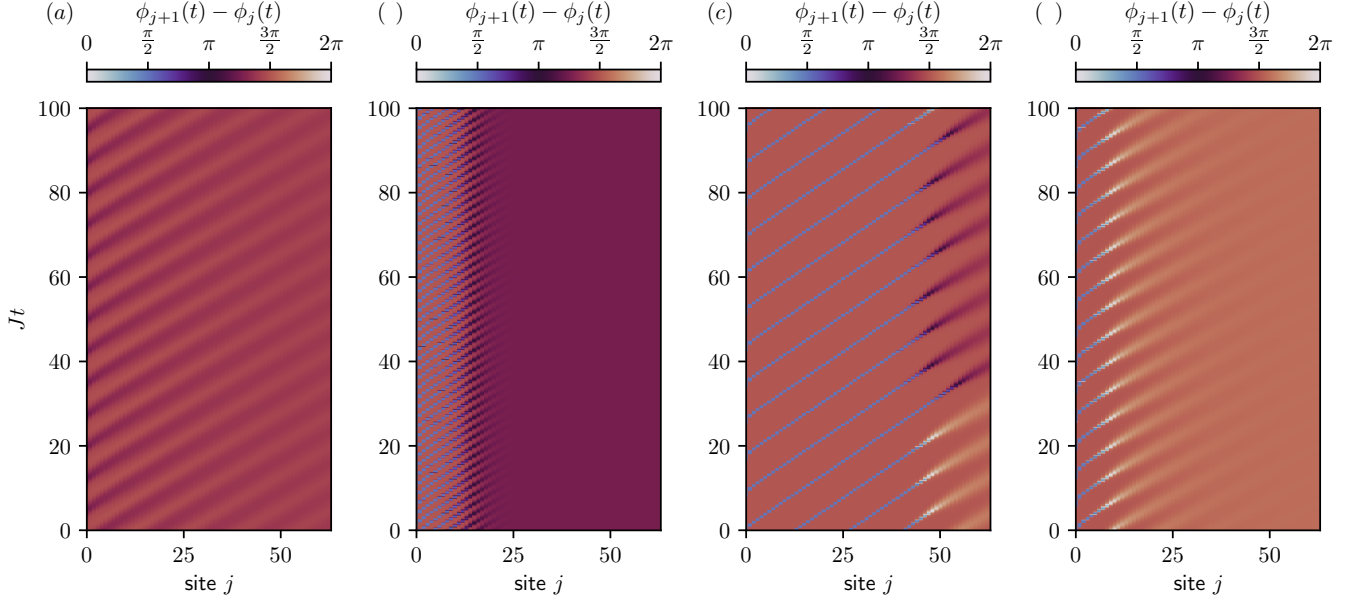


FIG. S5. (a) Phase II dynamics at the point $\kappa = 2.2$, $\gamma = 0.22$ (b) An example of a bistable solution with edge dynamics in Phase III for $\kappa = 1.25$, $\gamma = 0.4$. (c) Close-up of the periodic edge behavior in the chaotic phase for $\kappa = 2.2$, $\gamma = 0.7$ (d) Atypical dynamics near the Hatano-Nelson exceptional point at $\kappa = 2.1$, $\gamma = 0.8$.

$\phi = \pi$ are created at the edge and propagated into the bulk. These solitons continue until, at a seemingly arbitrary distance into the bulk, they are converted into boundaries between domains of CW and CCW rotation. This iterative domain wall generation results in the random walk in the phase of the bulk sites, as described above.

Approaching the Hatano-Nelson exceptional point from the dynamic phase, additional atypical dynamics can be exhibited beyond the features discussed thus far. As demonstrated in S5(d), the edge dynamics mixes together the periodic domain walls of the chaotic Phase IV (Right) and the nonuniform phase oscillations of Phase II.

-
- [S1] R. Hanai and P. B. Littlewood, Critical fluctuations at a many-body exceptional point, *Phys. Rev. Res.* **2**, 33018 (2020).
[S2] C. Weis, M. Fruchart, R. Hanai, K. Kawagoe, P. B. Littlewood, and V. Vitelli, Exceptional points in nonlinear and stochastic dynamics, [arXiv:2207.11667](https://arxiv.org/abs/2207.11667).
[S3] M. Fruchart, R. Hanai, P. B. Littlewood, and V. Vitelli, Non-reciprocal phase transitions, *Nature* **592**, 363 (2021).
[S4] C. P. Zelle, R. Daviet, A. Rosch, and S. Diehl, Universal Phenomenology at Critical Exceptional Points of Nonequilibrium $O(N)$ Models, *Phys. Rev. X* **14**, 021052 (2024).
[S5] G. Benettin, L. Galgani, A. Giorgilli, and J.-M. Strelcyn, Lyapunov Characteristic Exponents for smooth dynamical systems and for hamiltonian systems; A method for computing all of them. Part 2: Numerical application, *Meccanica* **15**, 21 (1980).
[S6] O. E. Rossler, An equation for hyperchaos, *Physics Letters A* **71**, 155 (1979).
[S7] O. E. Rössler, The chaotic hierarchy, in *A Chaotic Hierarchy* (WORLD SCIENTIFIC, 1991) pp. 25–47.